HHS Public Access

Author manuscript

Mol Cell Biomech. Author manuscript; available in PMC 2018 August 21.

Published in final edited form as:

Mol Cell Biomech. 2017 ; 14(3): 137–151. doi:10.3970/mcb.2017.014.137.

Comparison of Right Ventricle Morphological and Mechanical Characteristics for Healthy and Patients with Tetralogy of Fallot: An In Vivo MRI-Based Modeling Study

Dalin Tang[1,*,2], **Heng Zuo**[2,*], **Chun Yang**[2], **Zheyang Wu**[2], **Xueying Huang**[3], **Rahul H. Rathod**[4], **Alexander Tang**[4], **Kristen L. Billiar**[5], and **Tal Geva**[4]

[1]School of Biological Science & Medical Engineering, Southeast University, Nanjing, 210096, China

[2]Mathematical Sciences Department, Worcester Polytechnic Institute, Worcester, MA 01609

[3]School of Mathematical Sciences, Xiamen University, Xiamen, Fujian 361005, China

[4]Department of Cardiology, Boston Children's Hospital, Department of Pediatrics, Harvard Medical School, Boston, MA 02115 USA

[5]Department of Biomedical Engineering, Worcester Polytechnic Institute, MA 01609, USA

Abstract

Patients with repaired tetralogy of Fallot (TOF) account for the majority of cases with late onset right ventricle failure. Comparing TOF patients with healthy people may provide information to address this challenge. Cardiac magnetic resonance (CMR) data were obtained from 16 TOF patients (patient group, PG) and 6 healthy volunteers (healthy group, HG). At begin-of-ejection, better patient group (n=5, BPG) stress was very close to HG stress (54.7±38.4 kPa *vs.* 51.2±55.7 kPa, p=0.6889) while worse patient group (n=11, WPG) stress was 84% higher than HG stress (p=0.0418). Stress may be used as an indicator to differentiate BPG patients from WPG patients, with further validations.

Keywords

Heart modeling; cardiac mechanics; normal ventricle; right ventricle; tetralogy of Fallot

1 Introduction

With the recent development of modelling and imaging technology, computational mechanical analysis and computer-aided procedures have become more widely used in cardiac function analysis and patient-specific surgical design, replacing traditional empirical and often risky experimentation to examine the efficiency and suitability of various reconstructive cardiac procedures [McCulloch, Waldman, Rogers et al. (1992); Hunter,

Corresponding author: Dalin Tang, dtang@wpi.edu, 508-845-1575, fax: 508-831-5824.

*Co-first authors

Pullan and Smaill (2003); Pfeiffer, Tangney and Omens (2014); Fan, Yao, Yang et al. (2016)].

Tetralogy of Fallot (TOF) is a congenital heart defect which involves four anatomical abnormalities of the heart: pulmonary infundibular stenosis, overriding aorta, ventricular septal defect and right ventricular (RV) hypertrophy. With the introduction of TOF repair surgery, survival of TOF patients has increased substantially starting from the 80s. One recent report showed that long-term survival rate for repaired TOF patients decreased significantly after the first two decades of the initial repair [Nollert, Fischlein, Bouterwek et al. (1997)]. Pulmonary valve replacement (PVR) is one traditional surgical approach for repaired TOF patients with failing RV. Although the current PVR surgical approaches are meant to address pulmonary regurgitation issue, many patients do not experience an improvement in RV function and some show a decline after PVR [del Nido (2006); Geva, Gauvreau, Powell et al. (2010); McKenzie, Khan, Dietzman et al. (2014); Tweddell, Simpson, Li et al. (2012)].

In our previous publications [Tang, Yang, Geva et al. (2008); (2010)], computational RV/LV models were used in the comparison between regular PVR surgeries and PVR surgeries with RV remodeling, and PVR surgeries with RV remodeling were found to result in reduced stress/strain conditions in the patch area which may lead to improved recovery of RV function. In [Tang, Yang, Geva et al. (2011)], RV/LV models with different patch materials were constructed to evaluate the effect of patch materials on RV function. RV/LV models with contracting band were built to investigate the impact of band material stiffness variations, band length and active contraction [Yang, Tang, Geva et al. (2013)]. More recently, [Tang, Del Nido, Yang et al. (2016)] introduced RV/LV models with different zero-load diastole and systole geometries to reflect zero-stress sarcomere length changes in active contraction. These results indicated that computational models were powerful in the investigation of PVR surgeries.

In this study, CMR-based computational RV/LV models were constructed for 6 healthy volunteers and 16 TOF patients. The purposes of this study are: a) use RV/LV models to obtain RV morphological and mechanical parameters (circumferential and longitudinal curvatures, RV stress and strain) for healthy people which are lacking in the current literature; b) identify the differences in morphological and mechanical stress/strain characteristics between TOF patients and healthy people and see if these will help to differentiate better-outcome TOF patients from worse outcome TOF patients.

2 Data acquisition, models and methods

2.1 Data acquisition

This study was approved by the Boston Children's Hospital Committee on Clinical Investigation. CMR data were obtained from 22 people (9 male, 13 female; median age, 36.6 years; 16 with TOF, 6 healthy) previously enrolled in our RV surgical remodeling trial with written consent obtained [Geva, Gauvreau, Powell et al. (2010)]. For the 16 TOF patients, CMR data before and 6 months after PVR were available for model construction and analysis. Based on their RV ejection fraction (EF) changes, the patients were categorized

into two groups, the Better-Outcome Patient Group (BPG, n=5) which had positive RV EF changes (RV EF change: 3.94±2.20) and Worse-Outcome Patient Group (WPG, n=11) which had negative RV EF changes (RV EF change: −8.88±5.30, *p*-value: 0.00015). Demographic information, RV volumes, pressure conditions, and RV EF for the participants are summarized in Table 1. CMR acquisition procedures have been previously described [Tang, Yang, Geva et al. (2014)]. Each CMR data set consists of 30 time steps per cardiac cycle, and each time step data has 9–14 slices covering ventricles in ventricular short axis from base to apex. Three-dimensional RV/LV geometry and computational meshes were constructed following the procedures described in [Tang, Yang, Geva et al. (2011)]. Figure 1 shows selected CMR images from a TOF patient before the PVR surgery with segmented contours and re-constructed 3D RV/LV geometries. Our two-layer model construction and fiber orientation information were also provided [Hunter, Pullan and Smaill (2003); Sanchez-Quintana, Anderson and Ho (1996)].

Abbreviations: F: Female; M: male; EDV: end-diastolic volume; ESV: end-systolic volume; EF: ejection fraction.

2.2 The active anisotropic RV/LV models

The ventricular material was assumed to be hyperelastic, anisotropic, nearly-incompressible and homogeneous. Right Ventricular Outflow Tract (RVOT) material, patch and scar were assumed to be hyper-elastic, isotropic, nearly-incompressible and homogeneous. The governing equations for the structure models are:

$$\rho \frac{\partial^2 u_i}{\partial t^2} = \frac{\partial \sigma_{ij}}{\partial x_j}, i = 1, 2, 3 \quad (1)$$

$$\varepsilon_{ij} = \frac{1}{2}\left(\frac{\partial u_j}{\partial a_i} + \frac{\partial u_i}{\partial a_j} + \sum_l \frac{\partial u_l}{\partial a_i}\frac{\partial u_l}{\partial a_j}\right), i, j = 1, 2, 3 \quad (2)$$

Here $\boldsymbol{\sigma}$ is the stress tensor, $\boldsymbol{e}$ is Green's strain tensor, $\boldsymbol{u}$ is the displacement, and ρ is material density. The normal stress on the outer RV/LV surface was set to zero, and was set to the imposed RV/LV pressure conditions on the inner RV/LV surfaces:

$$P|_{RV} = P_{RV}(t), P|_{LV} = P_{LV}(t) \quad (3)$$

The Mooney-Rivlin model was used to describe the nonlinear anisotropic and isotropic material properties. The strain energy function for the isotropic modified Mooney-Rivlin model (for patch, scar tissue and RVOT material) was given by [Tang, Yang, del Nido et al. (2011, 2015)]:

$$W = c_1(I_1 - 3) + c_2(I_2 - 3) + D_1[\exp(D_2(I_1 - 3) - 1)] \quad (4)$$

$$I_1 = \sum C_{ii}, I_2 = \frac{1}{2}[I_i^2 - C_{ij}C_{ij}] \quad (5)$$

where I_1 and I_2 are the first and second strain invariants, $C = [C_{ij}] = X^T X$ is the right Cauchy–Green deformation tensor, $\boldsymbol{X}=[X_{ij}] = [\partial x_i/\partial a_j]$, (x_i) is current position, (a_i) is original position), and c_i and D_i are material parameters chosen to match experimental measurements [Tang, Yang, del Nido et al. (2015)]. The strain energy function for the anisotropic modified Mooney-Rivlin model was used for the ventricle tissue [Tang, Yang, del Nido et al. (2011); (2015)]:

$$W = c_1(I_1 - 3) + c_2(I_2 - 3) + D_1[\exp(D_2(I_1 - 3)) - 1] + K_1/(K_2)\exp[K_2(I_4 - 1)^2 - 1] \quad (6)$$

where $I_4 = C_{ij}(\mathbf{n}_f)_i(\mathbf{n}_f)_j$, C_{ij} is the Cauchy-Green deformation tensor, $\mathbf{n}_f$ is the fiber direction, K_1 and K_2 are material constants. The anisotropic strain-energy function with respect to the local fiber direction was given below [McCulloch, Waldman, Rogers et al. (1992)].

$$W = \frac{c}{2}(e^Q - 1) \quad (7)$$

$$Q = b_1 E_{ff}^2 + b_2(E_{cc}^2 + E_{rr}^2 + E_{cr}^2 + E_{rc}^2) + b_3(E_{fc}^2 + E_{cf}^2 + E_{fr}^2 + E_{rf}^2) \quad (8)$$

where E_{ff} is fiber strain, E_{cc} is cross-fiber in-plane strain, E_{rr} is radial strain, and E_{cr}, E_{fr} and E_{fc} are the shear components in their respective coordinate planes, C, b_1, b_2, and b_3 are parameters to be chosen to fit experimental data. It should be noted that Equations (7)–(8) were used because it is desirable to use local coordinate system to identify material parameters which are independent of fiber directions.

Biaxial mechanical testing of human myocardium was performed in Billiar's lab and results were reported in our previous paper [Tang, Yang, del Nido et al. (2015)]. Active contraction and relaxation were modeled by material stiffening and softening. In our material model, parameter values c_1, D_1 and C in equations (6) and (7) were adjusted at every CMR time step to match CMR-measured RV volume data for each patient. Fiber orientation was set the same way as in our previous papers (see Figure 1) [Hunter, Pullan and Smaill (2003); Sanchez-Quintana, Anderson and Ho (1996)].

2.3 Geometry-fitting mesh generation

Ventricles have complex irregular geometries which are challenging for mesh generation. A geometry-fitting mesh generation technique was developed to generate mesh for our models. Figure 1 (g) gives an illustration of RV/LV geometry between two slices. In each slice, “points” (ADINA mesh generation terms) were first defined based on the results of MRI segmentation. Then, “lines” were defined to divide the slice into geometry-fitting areas (called “surfaces” in ADINA). The neighboring slices were stacked to form “volumes”. Using this technique, the 3D RV/LV domain was divided into many small “volumes” to curve-fit the irregular ventricular geometry with patch and scar as inclusions. Finally, meshes were generated in each small volume. 3D surfaces, volumes and computational mesh were made under ADINA computing environment. Mesh analysis was performed by decreasing mesh size by 10% (in each dimension) until solution differences were less than 2%. The mesh was then chosen for our simulations.

2.4 Pre-shrink process

Numerical simulation needs to start from an initial condition where the initial ventricular geometry, pressure and stress/strain conditions of a working heart were provided. Since stress is hard to measure in vivo, our numerical simulations started from zero-load ventricular geometries with zero pressure and zero stress/strain distributions. Under in vivo condition, the ventricles were pressurized and the zero-load ventricular geometries were not known. In our model construction process, a pre-shrink process was applied to the in vivo begin-filling ventricular geometries to generate the starting shape (zero-load ventricular geometries) for the computational simulation. The initial shrinkage for the inner ventricular surface was 2–3% which was adjusted iteratively so that when begin-filling pressure was applied, the ventricles would match their in vivo morphology as much as possible. The ventricular out surface shrinkage was determined by volume conservation law so that the total ventricular wall volume was conserved. Without this pre-shrink process, the pressurized ventricle volume would be greater than its in vivo volume due to the initial expansion when pressure was applied.

2.5 Solution methods and morphological and stress/strain data for analysis

The RV/LV computational models (n=22) were constructed and solved by ADINA (ADINA R&D, Watertown, Mass) using finite elements and the New-Raphson iteration method. CMR-measured RV volume and pressure data were used to adjust model parameters so that model-predicted RV volume matched CMR-measure data.

Each ventricle model had 9–14 CMR slices. Every slice was divided into 4 quarters, each with equal inner wall circumferential length. Ventricular wall thickness (WT), circumferential curvature (C-cur), longitudinal curvature (L-cur), maximal principle stress (Stress-P_1) and maximal principle strain (Strain-P_1) were calculated at all nodal points (100 points per slice, 25 points per quarter). Their average values over the 25 points in each quarter provided the quarter values of these parameters which were collected for analysis. The formulas used for calculation of circumferential curvature (κ_C) at each point was

$$\kappa_c = \frac{x'y'' - x''y'}{(x'^2 + y'^2)^{3/2}} \quad (9)$$

The formulas used for calculation of longitudinal curvature (κ) at each point was

$$\kappa = \frac{\sqrt{(z''(t)y'(t) - y''(t)z'(t))^2 + (x''(t)z'(t) - z''(t)x'(t))^2 + (y''(t)x'(t) - x''(t)y'(t))^2}}{(x'^2(t) + y'^2(t) + z'^2(t))^{3/2}} \quad (10)$$

Details can be found from [Tang, Yang, del Nido et al. (2015)].

2.6 Statistical analysis

The mean and standard deviation values of RV volumes, WT, C-cur, L-cur, Stress-P_1 and Strain-P_1 were summarized by Table 2. Unpaired Student *t* test was used to compare mean RV volumes between different groups. Due to the small size of data, the quarter mean values were used in the analysis of RV wall thickness, curvatures, Stress-P_1 and Strain-P_1. Similar to what we did in [Tang, Yang, del Nido et al. (2015)], the Linear Mixed-Effect Model was used to take care of data dependence structure and make comparisons between different outcome groups.

3 Results

3.1 Comparison of geometrical parameters: TOF patients have noticeable differences in RV volume, L-cur and C-cur from healthy group

Table 2 summarized the average values of the geometrical and mechanical parameters from HG, BPG and WPG. These values were used in our group comparisons. Table 3 summarized and compared the average values of geometrical parameters (RV volume, wall thickness, L-cur and C-cur) between healthy group (HG) and patient group (PG = BPG + WPG). Bar plots of the average values are given in Figure 2 showing group differences. At the beginning of ejection, average Stress-P_1 of PG was 60.5% higher than that from HG (82.2±79.4 kPa *vs.* 51.2±55.7 kPa, p=0.1031). At the beginning of filling, mean Stress-P_1 of PG was 143.7% higher than that from HG (7.31±8.49 kPa *vs.* 3.00±2.30 kPa, p=0.0831). The high percentage should be discounted because the overall stress values were small. At begin of ejection, average Strain-P_1 from HG was 18% higher than that from PG. Noticing that average Strain-P_1 values from both HG and PG at begin-filling were about the same, higher strain from HG means that healthy ventricles had better contractibility, consistent with our expectations. RV volume was the parameter with the most noticeable difference between HG and PG. At the beginning of ejection, average PG RV volume was 87.9% higher than that from HG (344.9±131.3 cm^3 *vs.* 183.6±69.4 cm^3, p=0.0102). At the beginning of filling, average RV volume of PG was 151.5% higher than that from HG (204.2±97.9 cm^3 *vs.* 81.2±34.6 cm^3, p=0.0076). The high percentage difference at begin-filling was due to the fact that RV of PG contracted much less that HG.

C-cur and L-cur also showed large differences between HG and PG. At begin of ejection, mean PG C-cur was 35.8% lower than mean HG C-cur, and mean PG L-cur was 38.4% higher than mean HG L-cur. At begin of filling, average C-cur of PG was 22.9% lower than that from HG, and average L-cur of PG was 23.2% higher than that from HG. It is worth noting that the ratio of L-cur over C-cur for PG at begin-ejection is 2.29, compared to 1.06 for HG. At begin of filling, the ratio of L-cur over C-cur for PG is 1.90, compared to 1.19 for HG. RV WT did not show much difference between HG and PG.

3.2 HG may help differentiate BPG from WPG

Table 4 summarized and compared geometrical and mechanical parameter values of BPG and WPG to HG. Figure 3 gave the bar plots of average Stress-P_1, StrainP_1, RV volume, C-cur, L-cur and WT at begin-ejection, showing the differences among the three groups. Table 4 and Figure 3 showed that differences in wall thickness, C-cur and Strain-P_1 between BPG and WPG may not be very useful in differentiating BPG patients from WPG patients. Stress-P_1 from BPG was found to be closer to that from HG, compared to Stress-P_1 of WPG. At the beginning of ejection, mean Stress-P_1 of BPG was only 6.8% higher than that from HG (54.7±38.4 kPa *vs.* 51.2±55.7 kPa, p=0.6889), and the difference was not significant; while average Stress-P_1 of WPG was 84.1% higher than that of HG (94.3±89.2 kPa *vs.* 51.2±55.7 kPa, p=0.0418), and the difference was significant.

At the beginning of filling, average Stress-P_1 of BPG was 25% higher than that from HG (3.76±4.17 kPa *vs.* 3.00±2.30 kPa, p=0.5968), while average Stress-P_1 of WPG was 195.7% higher than that of HG (8.87±9.39 kPa *vs.* 3.00±2.30 kPa, p=0.0290). The results suggested that comparing patient's RV stress values with healthy RV stress values may help identify patients with possible better outcome.

Similarly, BPG RV volumes at Begin-Ejection were closer to HG RV volumes (263 cm^3 *vs.* 184 cm^3, 43% higher) compared to WPG volumes (382 cm^3 *vs.* 184 cm^3, 107% higher). BPG L-curvature was much greater than HG L-curvature at Begin-Ejection (1.42 *vs.* 0.86 1/cm, 65% higher) than WPG L-cur over HG (1.09 *vs.* 0.861/cm, 27% higher). Based on these results, RV volume and L-cur could be useful in identifying better-outcome patients.

4 Discussion

4.1 Modeling techniques for models based on in vivo data with complex geometry

It should be emphasized that the pre-shrink and mesh generation techniques presented in this paper are of general interest for models based on in vivo geometry and of complex structures. In vivo data of organs such as ventricles and arteries are under pressure and internal stress conditions. Most mechanical models require zero-stress geometry as their starting point for stress/strain calculations. Our pre-shrink pressure presented in this paper is a way to obtain the zero-load ventricle geometry as our model starting geometry. Without the shrinking process, as soon as pressure is added to the ventricle, the ventricle will be inflated and its volume will be greater than its in vivo size. This is a major difference between models based on in vivo data and models based on ex vivo data.

4.2 Motivation to construct models of healthy people

TOF patients have mixed results after PVR. It has remained challenging for the surgeons and clinicians to differentiate patients with better outcome from those with worse outcome. This work aims to determine if information from healthy people could be helpful in meeting that challenge. At the same time, general mechanical stress/strain and morphological information for healthy people will be good contributions since such data are still lacking in the current literature. It should be explained that our purpose is not only looking for differences between TOF patients and healthy people. We were also trying to find methods and indicators which could help us to separate BPG from WPG by using HG information. As the main result of this paper, it was found that BPG Stress-P_1 and HG Stress-P_1 were close to each other. In fact, they were not statistically different. This indicates RV stress could be a biomarker to be used for possible prediction of post-PVR outcome. RV volume and longitudinal curvature could serve the same purpose in a similar way.

4.3 Limitations

One limitation of this study is the small sample size which results in limited statistical power. The reason for the small sample size is the extensive amount of time required for constructing each computational model. Currently, it would take a trained modeling technician 2 weeks to generate one 3D patient-specific model. Thus, improving the model-building technique to make the process less labor-intensive and more clinically applicable will be a major effort for our future work.

Other limitations include: a) fluid-structure interactions can be added to obtain blood flow velocity and shear stress which can be also included in the investigation of predictors for good recovery after PRV; b) patient-specific and location-specific measurements of tissue mechanical properties (such as MRI with tagging) will be very desirable for improved accuracy of our models; c) inclusion of patient-specific fiber orientations; d) inclusion of pulmonary valve mechanics in the current model will be an important addition.

5 Conclusion

Our results indicated that RV stress from the better-outcome patient group was close to stress from the healthy group, and stress could be used as a potential indicator to differentiate BPG patients from WPG patients, with further validations.

Acknowledgments

This research was supported in part by National Heart, Lung and Blood Institute grants R01 HL089269 (PI del Nido, Tang, Geva), R01 HL63095 (PI del Nido) and 5P50HL074734 (PI: Geva). Tang's research was also supported in part by National Sciences Foundation of China grants 11672001, 81571691.

References

Del Nido PJ. Surgical Management of Right Ventricular Dysfunction Late after Repair of Tetralogy of Fallot: Right Ventricular Remodeling Surgery. Semin Thorac Cardiovasc Surg Pediatr Card Surg Annu. 2006; 9:29–34.

Fan L, Yao J, Yang C, Xu D, Tang D. Modeling Active Contraction and Relaxation of Left Ventricle Using Different Zero-load Diastole and Systole Geometries for Better Material Parameter

Estimation and Stress/Strain Calculations. MCB: Molecular & Cellular Biomechanics. 2016; 13(1): 44–68.

Geva T, Gauvreau K, Powell AJ, Cecchin F, Rhodes J, et al. Randomized trial of pulmonary valve replacement with and without right ventricular remodeling surgery. Circulation. 2010; 122(11 Suppl):S201–208. [PubMed: 20837914]

Hunter PJ, Pullan AJ, Smaill BH. Modeling total heart function. Annual Review of Biomedical Engineering. 2003; 5:147–177.

McCulloch AD, Waldman L, Rogers J, Guccione JM. Large-scale finite element analysis of the beating heart. Critical Reviews in Biomedical Engineering. 1992; 20:427–449. [PubMed: 1486784]

McKenzie ED, Khan MS, Dietzman TW, Guzm an-Pruneda FA, Samayoa AX, et al. Surgical pulmonary valve replacement: a benchmark for outcomes comparisons. Journal of Thoracic and Cardiovascular Surgery. 2014; 148:1450–1453. [PubMed: 24703628]

Nollert G, Fischlein T, Bouterwek S, Bohmer C, Klinner W, et al. Longterm survival in patients with repair of tetralogy of Fallot: 36-year follow-up of 490 survivors of the first year after surgical repair. Journal of The American College of Cardiology. 1997; 30:1374–1383. [PubMed: 9350942]

Pfeiffer RE, Tangney RJ, Omens HJ, McCulloch AD. Biomechanics of cardiac electromechanical coupling and mechanoelectric feedback. Journal of Biomechanical Engineering. 2014; 136:021007. [PubMed: 24337452]

Sanchez-Quintana D, Anderson R, Ho SY. Ventricular myoarchitecture in tetralogy of Fallot. Heart. 1996; 76:280–286. [PubMed: 8868990]

Tang D, Del Nido PJ, Yang C, Zuo H, Huang X, et al. Patient-Specific MRI-Based Right Ventricle Models Using Different Zero-Load Diastole and Systole Geometries for Better Cardiac Stress and Strain Calculations and Pulmonary Valve Replacement Surgical Outcome Predictions. PLoS One 2016. 2016 Sep 14.11(9):e0162986. 0162986.eCollection 2016. doi: 10.1371/journal.pone

Tang D, Yang C, del Nido PJ, Zuo H, Rathod RH, et al. Mechanical stress is associated with right ventricular response to pulmonary valve replacement in patients with repaired tetralogy of Fallot mechanical stress. Journal of Thoracic and Cardiovascular Surgery. 2015; 151:687–694. [PubMed: 26548998]

Tang D, Yang C, Geva T, del Nido PJ. Image-based patient-specific ventricle models with fluid-structure interaction for cardiac function assessment and surgical design optimization. Progress in Pediatric Cardiologyi. 2010; 30:51–62.

Tang D, Yang C, Geva T, del Nido PJ. Patient-specific MRI-based 3D FSI RV/LV/Patch models for pulmonary valve replacement surgery and patch optimization. Journal of Biomechanical Engineering. 2008; 130:041010. [PubMed: 18601452]

Tang D, Yang C, Geva T, del Nido PJ. Right ventricular local longitudinal curvature as a marker and predictor for pulmonary valve replacement surgery outcome: an initial study based on preoperative and postoperative cardiac magnetic resonance data from patients with repaired tetralogy of Fallot. Journal of Thoracic and Cardiovascular Surgery. 2014; 147:537–538. [PubMed: 24100105]

Tang D, Yang C, Geva T, Gaudette G, del Nido PJ. Multi-physics MRI-based two-layer fluid-structure interaction anisotropic models of human right and left ventricles with different patch materials: cardiac function assessment and mechanical stress analysis. Computers & Structures. 2011; 89:1059–1068. [PubMed: 21765559]

Tweddell JS, Simpson P, Li SH, Dunham-Ingle J, Bartz PJ, et al. Timing and technique of pulmonary valve replacement in the patient with tetralogy of Fallot. Journal of Thoracic and Cardiovascular Surgery. 2012; 15:27–33.

Yang C, Tang D, Geva T, Rathod R, Yamauchi H, et al. Using contracting band to improve right ventricle ejection fraction for patients with repaired tetralogy of Fallot: a modeling study using patient-specific CMR-based 2-layer anisotropic models of human right and left ventricles. Journal of Thoracic and Cardiovascular Surgery. 2013; 145:285–293. [PubMed: 22487437]

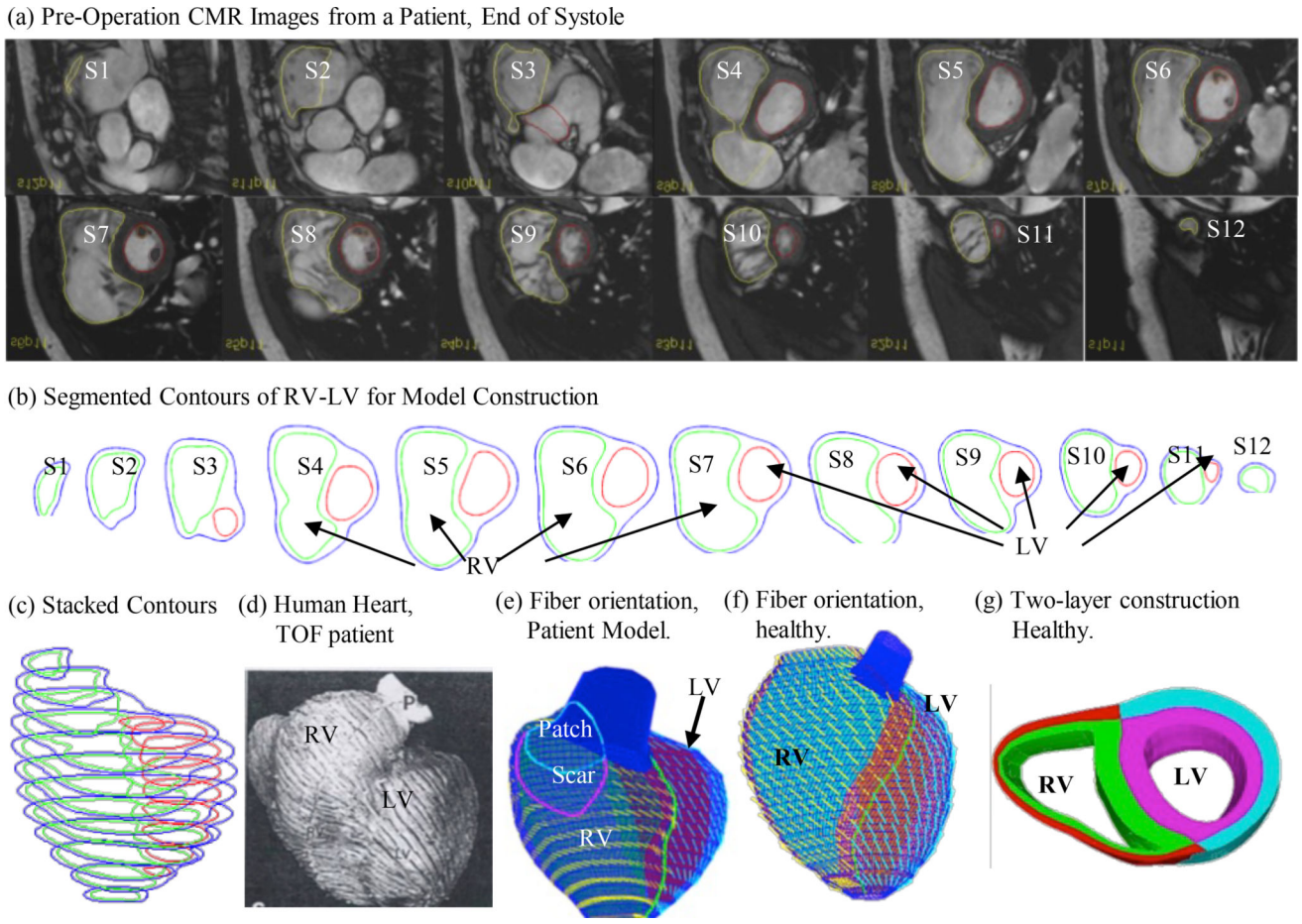

Figure 1.

Model construction process using CMR image slices from a TOF patient. (a) Pre-operative CMR images of a TOF patient; (b) segmented contours; (c) stacked contours; (d) fiber orientation from a human heart; (e–f) fiber orientation from RV/LV models of a TOF patient and a healthy volunteer; (g) two-layer construction.

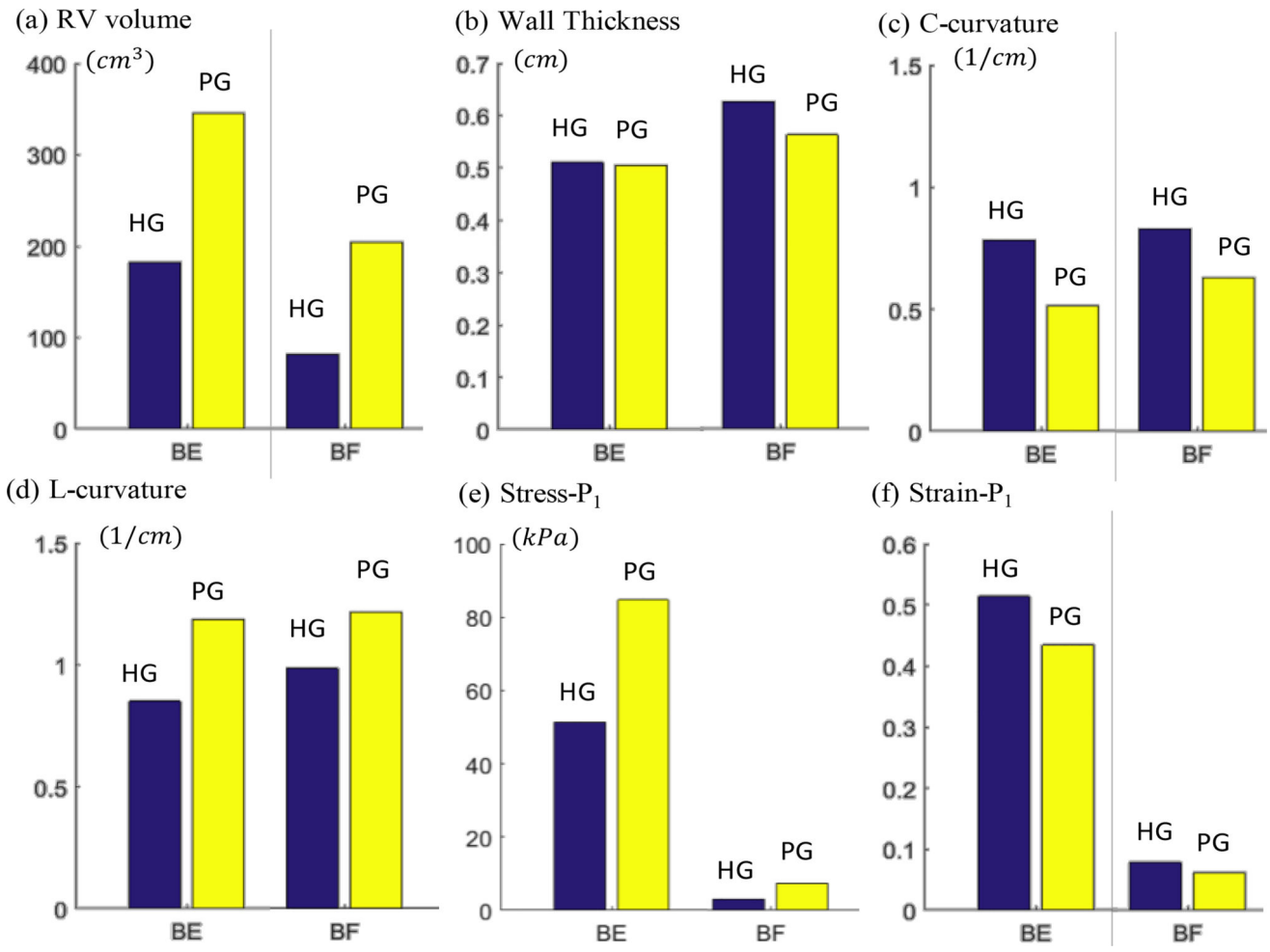

Figure 2.

Bar plots comparing RV volume, WT, C-cur, L-cur, Stress-P_1 and Strain-P_1 values from Healthy Group (HG) and Patient Group (HG) at Begin-Ejection (BE) and Begin-Filling (BF).

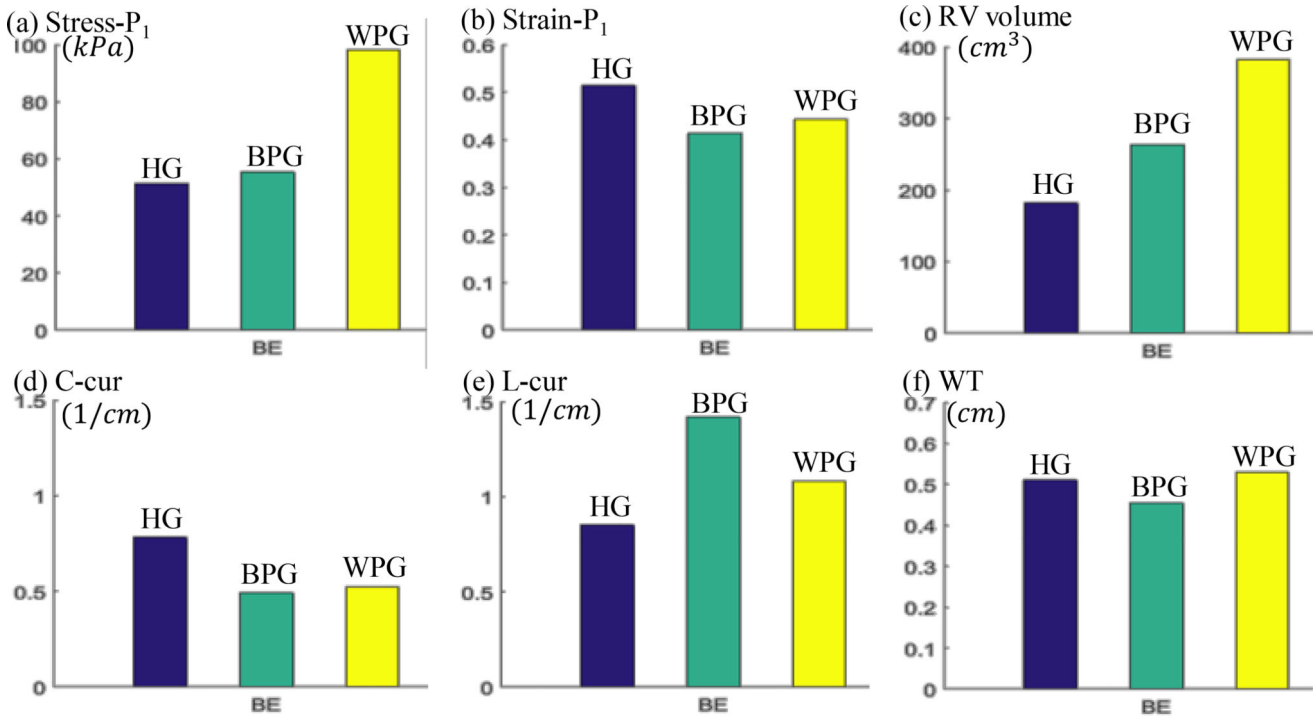

Figure 3.

Bar plots comparing average Stress-P_1, Strain-P_1, RV volume, C-cur, L-cur and WT values from Healthy Group (HG), Better-outcome Patient Group (BPG) and Worse-outcome Patient Group (WPG) at Begin-Ejection (BE). Blue: HG; Green: BPG; Yellow: WPG.

Table 1

Demographic and CMR data for healthy volunteers and TOF patients

Patient	Sex	Age (y)	Begin-Filling Pressure	Begin-Ejection Pressure	RV EDV (cm^3)	RV ESV (cm^3)	RV EF (%)	ΔEF (%)
Healthy Group (HG)								
H1	F	46.7	3.6	22	128.4	46.9	63	-
H2	M	23.6	5	27.9	226.6	105.4	53	-
H3	M	20.8	4.5	24	231.7	107.0	54	-
H4	M	19.4	3.9	23.8	213.5	94.2	56	-
H5	M	17.7	4.2	24.3	233.7	105.5	55	-
H6	M	6.7	4.3	24.8	67.6	28.2	58	-
Mean ± SD		22.5 ±13.2	4.25 ±0.48	24.5 ±1.93	183.6 ±69.4	81.2 ±34.6	56.5 ±3.62	-
Better-Outcome Patient Group (BPG)								
P1	M	22.5	21.6	31.4	406.9	254.5	37.5	1.4
P2	F	42.0	10	45	323.3	177.8	45.0	4.0
P3	F	14.3	3	29	204.0	104.3	48.8	5.6
P4	F	15.3	2	15	193.7	105.1	45.7	6.6
P5	M	17.0	3	27	188.3	108.3	42.5	2.0
Mean ± SD		22.2 ±11.5	7.92 ±8.29	29.5 ±10.7	263.2 ±97.7	150.0 ±66.2	43.9 ±4.22	3.92 ±2.24
Worse-Outcome Patient Group (WPG)								
P6	F	38.5	6	28	328.8	196.0	40.4	−3.4
P7	M	47.7	2	31	408.8	254.8	37.7	−2.6
P8	M	50.0	3	33	364.6	239.5	34.3	−2.9
P9	F	56.9	5	41	385.1	184.6	52.1	−18.0
P10	M	11.6	10	36	204.2	121.3	40.6	−8.4
P11	M	43.5	17	65	665.1	464.0	30.2	−15.2
P12	M	54.1	4	63	334.8	170.8	49.0	−7.0
P13	F	49.5	12	52	277.2	151.3	45.4	−5.0

Patient	Sex	Age (y)	Begin-Filling Pressure	Begin-Ejection Pressure	RV EDV (cm^3)	RV ESV (cm^3)	RV EF (%)	ΔEF (%)
P14	M	17.8	2	30	365.0	178.0	51.2	−9.5
P15	F	44.6	11	50	299.0	186.0	37.8	−12.3
P16	F	45.3	9	49	571.1	371.3	35.0	−13.4
Mean ± SD		41.8 ±14.4	7.36 ±4.82	43.5 ±13.2	382.2 ±131	228.9 ±102	41.2 ±7.27	−8.88 ±5.29

Table 2

Summary of mean geometric and stress/strain parameter values at begin of ejection

	WT (cm)	C-cur (1/cm)	L-cur (1/cm)	RV EDV (cm^3)	Stress-P_1 (kPa)	Strain-P_1
HG						
H1	0.35	1.15	0.87	125.2	70.2	0.63
H2	0.68	0.68	0.56	227.1	51.6	0.58
H3	0.64	0.77	0.68	226.7	36.3	0.40
H4	0.51	0.62	0.61	213.1	56.0	0.39
H5	0.57	0.57	1.27	232.6	45.9	0.57
H6	0.31	0.90	1.11	66.37	48.0	0.51
Mean ± SD	0.51 ±0.15	0.81 ±0.19	0.85 ±0.29	183.6 ±69.4	51.3 ±11.4	0.51 ±0.10
BPG						
P1	0.39	0.47	1.24	406.9	56.9	0.29
P2	0.47	0.43	0.96	323.3	82.4	0.44
P3	0.48	0.50	1.20	204.0	61.9	0.48
P4	0.42	0.53	1.84	193.7	33.5	0.46
P5	0.51	0.53	1.85	188.3	42.0	0.40
Mean ± SD	0.45 ±0.05	0.49 ±0.04	1.42 ±0.40	263.2 ±97.7	55.3 ±18.9	0.41 ±0.08
WPG						
P6	0.34	0.39	0.77	328.8	65.3	0.43
P7	0.65	0.37	1.01	408.8	41.0	0.33
P8	0.49	0.54	1.54	364.6	64.1	0.36
P9	0.48	0.42	0.91	385.1	172.1	0.66
P10	0.41	1.34	1.32	204.2	82.9	0.49
P11	0.80	0.36	0.59	665.1	82.4	0.23
P12	0.71	0.44	0.72	334.8	83.1	0.42
P13	0.45	0.46	0.97	277.2	191.7	0.66

	WT (cm)	C-cur (1/cm)	L-cur (1/cm)	RV EDV (cm^3)	Stress-P_1 (kPa)	Strain-P_1
P14	0.43	0.65	1.60	365.0	65.4	0.44
P15	0.46	0.44	1.23	299.0	154.3	0.51
P16	0.59	0.33	1.25	571.1	76.2	0.34
Mean ± SD	0.53 ±0.14	0.52 ±0.29	1.08 ±0.33	382.2 ±131.1	98.0 ±50.1	0.44 ±0.13

Abbreviations: WT: wall thickness; C-cur: circumferential curvature; L-cur: longitudinal curvature

Table 3

Comparison of RV volumes, geometric parameters, and stress/strain values between healthy group (HG) and patient group (PG=BPG+WPG) at begin of ejection and begin of filling.

	Begin of Ejection			Begin of Filling		
	PG	HG	*P* value	PG	HG	*P* value
RV volume(cm^3)	344.9±131.3	183.6±69.4	0.0102	204.2±97.9	81.2±34.6	0.0076
WT (cm)	0.51±0.24	0.51±0.30	0.9315	0.57±0.27	0.64±0.32	0.3616
C-cur (1/cm)	0.52±1.21	0.81±1.05	0.0237	0.64±1.23	0.83±0.51	0.1519
L-cur (1/cm)	1.19±1.21	0.86±0.71	0.0756	1.22±1.22	0.99±0.66	0.2585
Stress-P_1 (kPa)	82.2±79.4	51.2±55.7	0.1031	7.31±8.49	3.00±2.30	0.0831
Strain-P_1	0.43±0.19	0.51±0.17	0.1486	0.06±0.07	0.07±0.06	0.5376

Values are expressed as mean±standard deviation.

Abbreviations are the same as in Table 2.

Mol Cell Biomech. Author manuscript; available in PMC 2018 August 21.

Table 4

Comparison of geometric and stress/strain mean values between healthy group (HG) and patient groups (better-outcome patient group (BPG), worse-outcome patient group (WPG)).

	Begin of Ejection			**Begin of Filling**		
	BPG	HG	*P* value	BPG	HG	*P* value
RV volume 3) (cm^3)	263.2±97.7	183.6±69.4	0.1482	150.0±66.2	81.2±34.6	0.0534
WT (cm)	0.45±0.20	0.52±0.30	0.4441	0.50±0.21	0.64±0.32	0.1099
C-cur (1/cm)	0.49±0.26	0.81±1.05	0.0094	0.63±0.34	0.83±0.51	0.0082
L-cur (1/cm)	1.42±1.40	0.86±0.71	0.0263	1.58±1.56	0.99±0.66	0.0420
Stress-P_1 (kPa)	54.7±38.4	51.2±55.7	0.6889	3.76±4.17	3.00±2.30	0.5968
Strain-P_1	0.41±0.18	0.51±0.17	0.1042	0.03±0.02	0.07±0.06	0.1047
	WPG	HG	*P* value	WPG	HG	*P* value
RV volume (cm^3)	382.1±131.1	183.6±69.4	0.0038	228±102.4	81.2±34.6	0.0041
WT (cm)	0.53±0.26	0.52±0.30	0.8150	0.60±0.29	0.64±0.32	0.6508
C-cur (1/cm)	0.54±1.45	0.81±1.05	0.0709	0.64±1.46	0.83±0.51	0.2427
L-cur (1/cm)	1.09±1.11	0.86±0.71	0.2006	1.07±1.00	0.99±0.66	0.6194
Stress-P_1 (kPa)	94.3±89.2	51.2±55.7	0.0418	8.87±9.39	3.00±2.30	0.0290
Strain-P_1	0.43±0.20	0.51±0.17	0.2603	0.08±0.07	0.07±0.06	0.9860